Rare Metal Materials and Engineering
Volume 55, Issue 2, February 2026
Available online at www.rmme.ac.cn

Science Press

Cite this article as: Wang Shuyan, Zhou Yuting, Du Ruibo, et al. Effect of Initial Microstructure States on Flow Behavior of Al-Zn-Mg-Cu Alloy During Hot Tensile Deformation[J]. Rare Metal Materials and Engineering, 2026, 55(02): 302-314. DOI: https://doi.org/10.12442/j.issn.1002-185X.20250100.

ARTICLE

Effect of Initial Microstructure States on Flow Behavior of Al-Zn-Mg-Cu Alloy During Hot Tensile Deformation

Wang Shuyan[1], Zhou Yuting[2], Du Ruibo[3], Long Shuai[1,3], Lin Haitao[1], Wang Shaoyang[2]

[1] Southwest Aluminum Group Co., Ltd, Chongqing 401326, China; [2] Chengdu Aircraft Industry (Group) Co., Ltd, Aviation Industry Corporation of China Ltd, Chengdu 610073, China; [3] College of Metallurgy and Power Engineering, Chongqing University of Science and Technology, Chongqing 401331, China

Abstract: To investigate the influence of Al-Zn-Mg-Cu alloy with as-homogenized and as-rolled initial microstructures on the tensile flow behavior, isothermal tensile tests were conducted on a GLEEBLE-3500 isothermal simulator at temperatures of 380–440 °C and strain rates of 0.05–1 s^{-1}. The Johnson-Cook model, Hensel-Spittel model, strain-compensated Arrhenius model, and critical fracture strain model were established. Results show that through the evaluation of the models using the correlation coefficient (R) and the average absolute relative error, the strain-compensated Arrhenius model can represent the flow behavior of the alloy more accurately. Shear bands are more pronounced in the as-homogenized specimens, whereas dynamic recrystallization is predominantly observed in as-rolled specimens. Fracture morphology analysis reveals that a mixed fracture mechanism is prevalent in the as-homogenized specimen, whereas a ductile fracture mechanism is predominant in the as-rolled specimen. The processing maps indicate that the unstable region is reduced in the as-rolled specimens compared with that in the as-homogenized specimens. The optimal hot working windows for the as-homogenized and as-rolled specimens are determined as 410–440 °C/0.14–1 s^{-1} and 380–400 °C/0.05–0.29 s^{-1}, respectively.

Key words: Al-Zn-Mg-Cu alloy; tensile flow behavior; microstructure; constitutive modelling; processing map

1 Introduction

Al-Zn-Mg-Cu alloy is favored for aerospace and transportation fields due to its excellent mechanical properties, strong resistance against stress corrosion cracking, and exceptional fracture toughness[1–3]. Thermal processes, such as hot rolling and forging, are essential for the fabrication of aluminum alloy components[4–5]. In practical production, Al-Zn-Mg-Cu alloy thick plates are formed through multi-pass hot rolling[6]. As rolling deformation accumulates, the coarse secondary-phases are fragmented, the substructure within the grains increases, and the recovery as well as recrystallization is easier to activate, which affects the flow features of the subsequent deformation process. Furthermore, the rolled plate is subjected to tensile stress at 1/2 of thickness in the rolling direction; the stress state is close to unidirectional tensile deformation state, which is one of the main causes of crack defects. Ensuring reliable forming quality requires an understanding of flow behavior, microstructure evolution, and workability restrictions in vulnerable regions across various deformation states during rolling processes under tensile stress at high temperatures. Isothermal tensile simulation provides feasibility for study of the tensile stress and microstructure in the approximate rolling process. Moreover, in the actual production process, hot rolling does not directly shape the homogenized ingot into the final structural component. The ingot is in the intermediate-rolling state when it is rolled from 450 mm to 195 mm in thickness. During the process of further deformation based on the thickness of 195 mm, the improper selection of processing parameters is likely to cause defects, such as cracking, which will affect the forming quality. Therefore, studying the hot deformation behavior of the alloy at different states and selecting the optimal hot-processing parameter window are of guiding significance to evaluate the alloys during secondary deformation.

Received date: March 03, 2025
Corresponding author: Long Shuai, Ph. D., College of Metallurgy and Power Engineering, Chongqing University of Science and Technology, Chongqing 401331, P. R. China, E-mail: longshuai@cqust.edu.cn

Flow behavior is usually described by reliable flow constitutive models, which can also provide effective theoretical guidance for accurate numerical simulations[7–9]. Recently, the flow constitutive model of the Al-Zn-Mg-Cu alloy has been widely studied. Yao et al[10] conducted isothermal compression tests on as-rolled 7050 alloy, developing a strain-compensated Arrhenius model with a relative average error of 8.61% and an average thermal activation energy of 181.2 kJ·mol^{-1}. Tan et al[11] established the original Johnson-Cook constitutive model, Khan-Liu model, and modified Johnson-Cook model for 7050-T7451 alloy. The findings suggest that not all models accurately describe the flow behavior of 7050-T7451 alloys, and the modified Johnson-Cook model demonstrates superior predictive accuracy for the hot tensile flow behavior. Wang et al[12] constructed hot processing maps and identified unstable regions in the range of 300–400 °C/0.001–0.02 s^{-1} for thermal compression tests of in-situ reinforced 7050 aluminum alloy with 5wt% TiB_2. The processing map has emerged as an effective tool for elucidating the intrinsic workability of aluminum alloys. Wang et al[13] used traditional hot processing maps in conjunction with 3D hot processing maps to identify the unstable range of AA7050 aluminum alloy, which lies between 360 – 420 ° C/0.1 – 10 s^{-1}. Chen et al[15] used the processing maps to pinpoint tensile unstable zones in the rolled 7050 aluminum alloy at high strain rates (>10^{-3} s^{-1}) and temperatures of 340–380 °C.

It is noteworthy that the constitutive models to predict flow stress and the hot processing maps to identify the unstable regions have been widely applied to the hot deformation processes of various metal materials. The development of appropriate constitutive models and the selection of optimized hot processing windows are critical for optimizing the process parameters and controlling the material forming behavior.

However, the hot deformation characteristics and hot processing maps of aluminum alloys of the same grade but featuring distinct microstructural states are rarely reported. For instance, Li et al[14] investigated the softening behavior of as-homogenized and pre-rolled AA2060 aluminum alloy through isothermal compression experiments. The results showed that the pre-rolled specimens exhibited lower flow stress and lower thermal activation energy under the same deformation conditions. The hot processing maps indicated a significant reduction in the instability zone for the pre-rolled specimens, compared with that at the homogeneous state. The recrystallization fraction of the pre-rolled specimens was higher than that of the as-homogenized specimens, and meta-dynamic recrystallization occurred during the deformation of the pre-rolled specimens. Chen et al[15] studied the thermal compressive deformation characteristics of 7085 aluminum alloy at homogenized and solution-treated states. The processing maps revealed that the solution-treated specimen showed greater power dissipation efficiency and a wider unstable region. Therefore, elucidating tensile flow behavior, constitutive models, and processing maps of Al-Zn-Mg-Cu alloys with varying initial microstructures is essential for optimizing the industrial production.

In this research, the flow stress characteristics of homogenized and hot-rolled Al-Zn-Mg-Cu aluminum alloys were analyzed via isothermal tensile tests. The influence of the initial microstructure on flow behavior, microstructure evolution, and fracture mechanisms was analyzed. The Johnson-Cook, Hensel-Spittel, and strain-compensated Arrhenius models were established for the alloy at different states and validated using correlation coefficient (R) and average absolute relative error (AARE) metrics. Processing maps were constructed for alloys of different microstructures to identify optimal hot working regions.

2 Experiment

The received Al-Zn-Mg-Cu alloys consist of a homogenized ingot and a hot-rolled thick plate (supplied by Southwest Aluminum. Co., Ltd). The ingot was subjected to a two-stage homogenization treatment. Firstly, it was held at 450 °C for 15 h, then held at 480 °C for 24 h, and finally cooled in the furnace. After that, it was pre-rolled through multi-passes of hot rolling at 400 °C from the initial thickness of 460 mm to 195 mm. The reduction amount was increased by 5 mm for every two passes, and the reduction amount of the first pass was 10 mm. Then, it was naturally aged at room temperature for over 3 months. The actual chemical composition of Al-Zn-Mg-Cu alloy is listed in Table 1. The microstructures were observed by optical microscope (OM) and scanning electron microscope (SEM). 3D OM images, SEM images at backscattered electron (BSE) mode, and corresponding energy dispersive spectroscope (EDS) mappings of the as-homogenized and as-rolled specimens are shown in Fig. 1. ND, TD, and RD indicate the normal direction, transverse direction, and rolling direction, respectively. Fig. 2a–2b depict the sampling locations of hot-rolled specimens and the geometry of the specimens, respectively. Before the tensile test, the rough surfaces of the tensile specimens were sanded using 400#–800# sandpaper. A GLEEBLE-3500 isothermal simulator was employed for the isothermal tensile tests. Fig. 2c illustrates the uniaxial thermal tensile process. The specimens were heated to 380, 410, and 440 °C at a heating rate of 10 °C/s using resistance heating, followed by holding for 3 min to eliminate temperature gradients. Subsequently, tensile strain rates of 0.05, 0.5, and 1 s^{-1} were applied during the tensile process. After fracture, the specimens were rapidly quenched by compressed argon.

Specimens with dimensions of 20 mm×20 mm×5 mm were taken from the ingot by wire-electrical discharge machining. After cleaning the oil stains on the surface by acetone solution, the actual chemical composition was measured by the optical emission spectrometer. As shown in Fig. 2c, the fractured tensile specimens were cut by wire-electrical machine along the tensile direction. The observation surfaces

Table 1 Chemical composition of Al-Zn-Mg-Cu alloy

Zn	Mg	Cu	Cr	Fe	Mn	Ti	Si	Al
5.62	2.23	1.51	0.21	0.16	0.05	0.02	0.07	Bal.

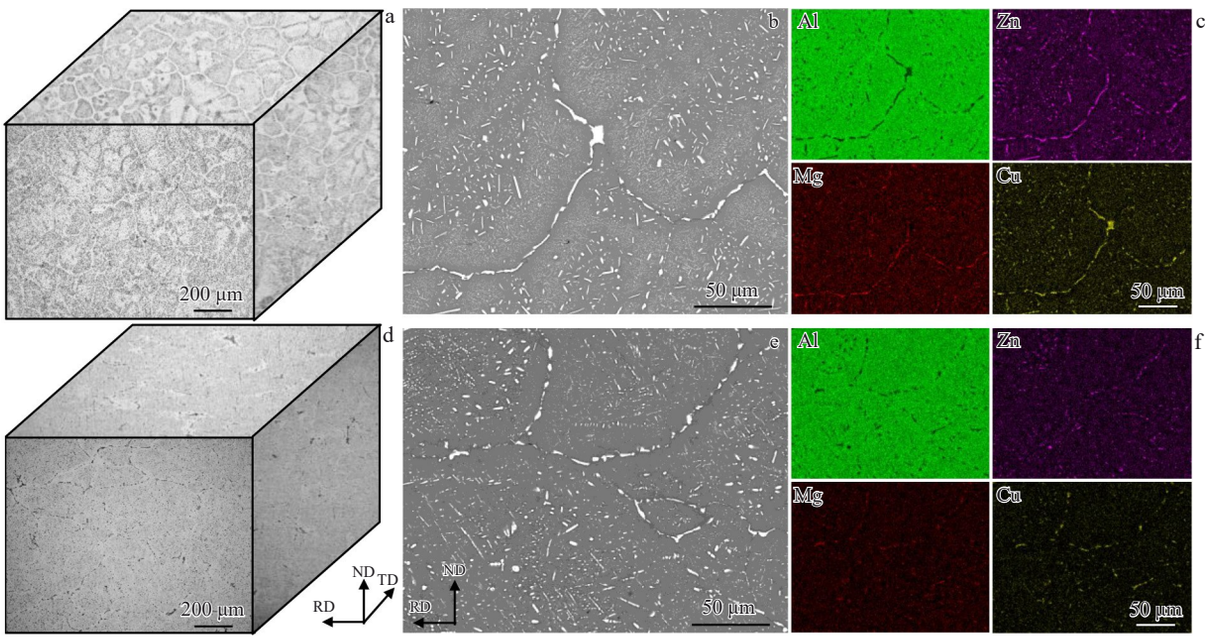

Fig.1 Initial 3D OM images (a, d), SEM-BSE images along RD-ND (b, e), and corresponding EDS mappings (c, f) of as-homogenized specimen (a–c) and as-rolled specimen (d–f)

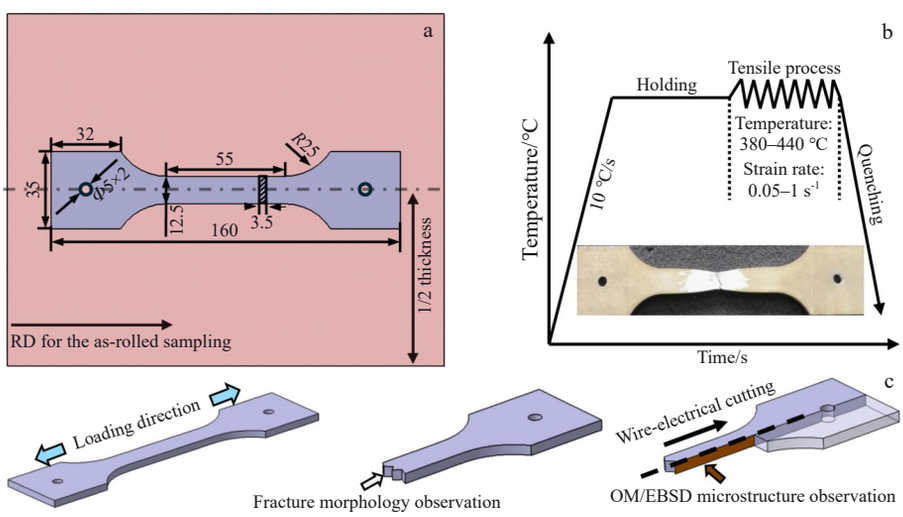

Fig.2 Schematic diagram of sampling position of specimen (a); flow chart of tensile test (b); schematic diagrams of tensile test and microstructure observation positions (c)

were sequentially sanded with 400# – 3000# sandpaper and mechanically polished. For OM observation, the polished surfaces were then etched by Keller reagent (2 mL HNO_3, 1 mL HF, 1 mL HCl, and 40 mL H_2O) for 10 s. For electron back-scattered diffraction (EBSD) characterization, the polished surfaces were further electrochemically polished in the solution of 30 mL HNO_3 and 70 mL CH_3OH at −30 °C for 30 s. SEM and EBSD characterizations were performed using a JSM-7800F field emission SEM.

3 Results and Discussion

3.1 True stress-true strain curves

Fig. 3 shows the true stress-true strain curves of different specimens under different deformation conditions. At both the as-homogenized and as-rolled states, the flow stress is negatively correlated with the deformation temperature at a certain strain rate, and it is positively correlated with the strain rate at a certain temperature. At the initial deformation stage, due to the work hardening, the flow stress rapidly rises to reach a peak value. As the strain further increases, dynamic softening effect intensifies, causing the flow stress to decrease gradually. Eventually, the onset of necking phenomenon leads to internal damage within the specimen, resulting in a reduction in flow stress and ultimately leading to fracture.

It is worth noting that the as-rolled specimens show better elongation compared with the as-homogenized specimens,

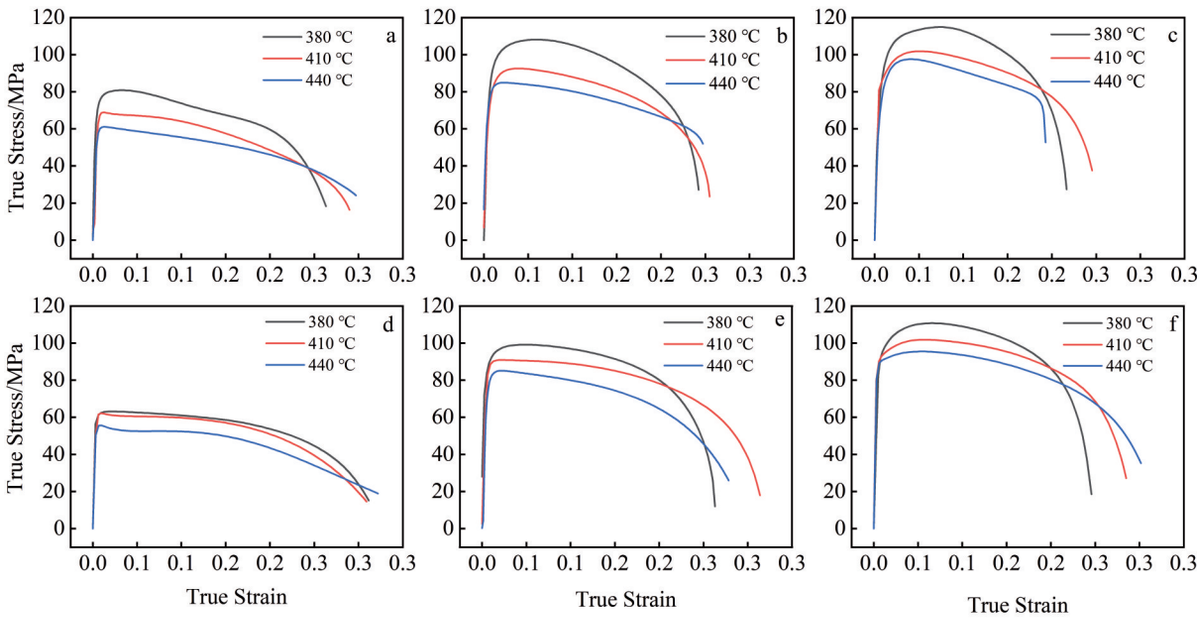

Fig.3 True stress-true strain curves of as-homogenized (a–c) and as-rolled (d–f) Al-Zn-Mg-Cu alloys at $\dot{\varepsilon}$=0.05 s^{-1} (a, d), $\dot{\varepsilon}$=0.5 s^{-1} (b, e), and $\dot{\varepsilon}$= 1 s^{-1} (c, f)

whereas the yield strength and ultimate tensile strength of the as-homogenized specimens are higher. As shown in Fig. 1a–1c, the as-homogenized specimen contains a large number of equiaxed grains. Coarsened secondary-phases are visible at the grain boundaries, and EDS analysis reveals that these secondary-phases contain elements Zn, Mg, and Cu of high concentrations. This is the primary reason that the as-homogenized specimens exhibit higher ultimate tensile strength. Fig. 1d–1f illustrate the grain structure parallel to RD within the as-rolled specimens, presenting fragmented and discontinuous morphology of the grain boundaries. This may result in a higher elongation when the tensile test is conducted along RD.

3.2 Constitutive modelling

3.2.1 Fracture strain model

The Johnson-Cook model is widely used in engineering due to its clear physical significance of parameters. Besides, it can provide accurate flow stress predictions under specific reference conditions[16–18]. The Hensel-Spittel model incorporates multiple parameters, comprehensively considering the coupling effects of temperature, strain rate, and strain, and making it applicable and straightforward[19–22]. The Arrhenius constitutive model has gained widespread application due to its ability to predict flow stress over large deformation ranges and its incorporation of the activation energy Q parameter to characterize the deformation mechanisms in the thermal deformation process of materials[23–25].

The abovementioned constitutive models have primarily focused on the flow stress prediction within a consistent strain range, neglecting the fracture behavior. For the tensile tests, the fracture strain varies under different deformation conditions, which requires a modified fracture strain model. An empirical formula is employed to obtain the fracture strain (ε_f) of the specimen under different deformation conditions, as expressed by Eq.(1):

$$\varepsilon_f = \ln\frac{A_0}{A_f} \tag{1}$$

where A_0 represents the initial cross-section area of the specimen, and A_f denotes the minimum cross-section area at the fracture notch. The fracture strain values of different specimens are provided in Table 2.

By establishing multivariate polynomial coupling relationships among temperature, strain rate, and fracture strain, the expression for fracture strain is derived as Eq. (2). Fig. 4 presents the fitted relationship of fracture strain of as-homogenized and as-rolled specimens under deformation conditions. The variables for as-homogenized and as-rolled specimens in Eq.(2) are obtained and listed in Table 3.

$$\varepsilon_f = a + b\ln\tilde{T}_i + c\ln\dot{\varepsilon}^* + d\ln\tilde{T}_i\ln\dot{\varepsilon}^* + e(\ln\tilde{T}_i)^2 + f(\ln\dot{\varepsilon}^*)^2 \tag{2}$$

where $\dot{\varepsilon} = \dot{\varepsilon}/\dot{\varepsilon}_{ref}$ is the dimensionless strain rate with $\dot{\varepsilon}$ as the strain rate and $\dot{\varepsilon}_{ref}$ as the reference strain rate; $\tilde{T}$ is introduced by (T/T_{min}) with T and T_{min} as the actual and minimum temperatures, respectively; i indicates the ith element; a, b, c,

Table 2 Values of fracture strain under different deformation conditions

Specimen state	Temperature/°C	Strain rate/s^{-1}		
		0.05	0.5	1
As-homogenized	380	0.2010	0.2210	0.1812
	410	0.2210	0.2310	0.2020
	440	0.2600	0.2400	0.1840
As-rolled	380	0.2423	0.2153	0.1812
	410	0.2497	0.2430	0.2218
	440	0.1788	0.1904	0.1919

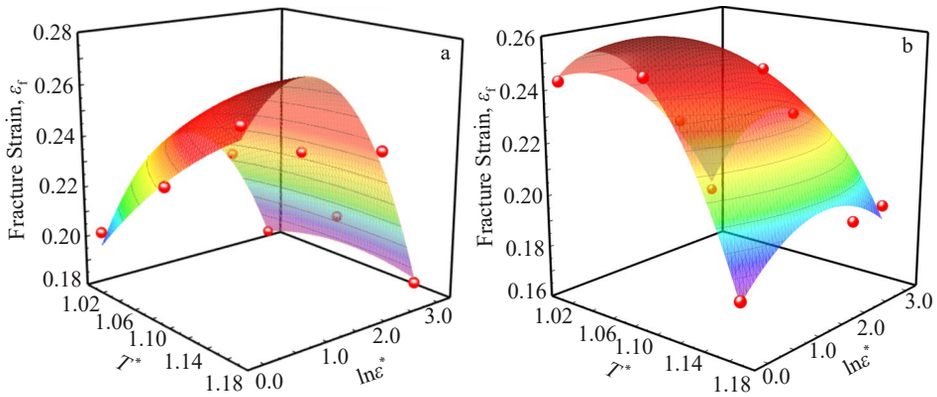

Fig.4 Fitted relationship diagrams of fracture strain of as-homogenized (a) and as-rolled (b) Al-Zn-Mg-Cu alloys under deformation conditions

Table 3 Parameter values of fracture strain polynomial of as-homogenized and as-rolled Al-Zn-Mg-Cu alloys

Parameter	*a*	*b*	*c*	*d*	*e*	*f*
As-homogenized	−1.18	2.24	0.18	−0.12	−0.86	−0.020
As-rolled	−6.43	12.80	−0.14	−0.14	−6.12	−0.008

d, *e*, and *f* are fitting parameters.

3.2.2 Johnson-Cook model

The Johnson-Cook model[26] can predict the flow stress of materials under high-temperature deformation conditions by incorporating three distinct components: strain hardening, strain rate, and thermal softening[27]. Its expression is as follows:

$$\sigma = (A + B\varepsilon^n)(1 + C\ln\dot{\varepsilon}^*)(1 - T^{*m}) \quad (3)$$

where σ is the flow stress (MPa); ε is the plastic strain; $A + B\varepsilon^n$ represents the strain-hardening part with A as the yield stress, B as the strain-hardening strength, and n as the strain-hardening coefficient; $1 + C\ln\dot{\varepsilon}^*$ is the strain rate term with C as the strain rate constant and $\dot{\varepsilon}^*$ as the dimensionless strain rate; $1 - T^{*m}$ term describes the thermal softening effect with m as the temperature-related softening coefficient and T^* as the dimensionless temperature term introduced by $T - T_{ref}$ (T and T_{ref} are the actual and reference temperatures, respectively).

Lin et al[28] proposed a modified Johnson-Cook model, where the strain hardening part is fitted with a trinomial, while the thermal softening part contains the effects of strain rate and temperature, as follows:

$$\sigma = (A + B_1\varepsilon + B_2\varepsilon^2 + B_3\varepsilon^3)(1 + C_1\ln\dot{\varepsilon}^*) \times \exp[(\lambda_1 + \lambda_2\ln\dot{\varepsilon}^*)T^*] \quad (4)$$

where A, B_1, B_2, C_1, λ_1, and λ_2 are material constants.

3.2.3 Hensel-Spittel model

The Hensel-Spittel model can predict the flow stress using the power law dependence among temperature, strain rate, strain, and stress. Its expression is as follows:

In the Johnson-Cook model, a lower strain rate is typically selected as the reference strain rate[29]. In this research, 380 °C/0.05 s^{-1} was set as the reference condition to determine the parameters of the model, and the solving process of parameters is as follows.

(1) Under the reference deformation conditions, Eq.(4) can be simplified as Eq.(5):

$$\sigma = A + B_1\varepsilon + B_2\varepsilon^2 + B_3\varepsilon^3 \quad (5)$$

Fitting the data points through a trinomial can obtain the coefficients A, B_1, and B_2.

(2) With fixed temperature, Eq.(4) is converted to Eq.(6), as follows:

$$\frac{\sigma}{A + B_1\varepsilon + B_2\varepsilon^2 + B_3\varepsilon^3} - 1 = C_1\ln\dot{\varepsilon}^* \quad (6)$$

Substituting A, B_1, and B_2 into Eq. (6), the relationship between $\sigma/(A + B_1\varepsilon + B_2\varepsilon^2 + B_3\varepsilon^3) - 1$ and $\ln\dot{\varepsilon}^*$ is plotted and a linear fitting is performed to obtain the slope as the value of C_1 parameter. All the solving processes are shown in Fig.5.

(3) After shifting and taking logarithms on the terms, Eq.(4) is transformed into Eq. (7). Then, $\lambda = \lambda_1 + \lambda_2\ln\dot{\varepsilon}^*$. The relationship between $\ln[\sigma/(A + B_1\varepsilon + B_2\varepsilon^2 + B_3\varepsilon^3)(1 + C_1\ln\dot{\varepsilon}^*)]$ and T^* at different strain rates is revealed in Step 2 in Fig.5.

$$\ln\frac{\sigma}{(A + B_1\varepsilon + B_2\varepsilon^2 + B_3\varepsilon^3)(1 + C_1\ln\dot{\varepsilon}^*)} = (\lambda_1 + \lambda_2\ln\dot{\varepsilon}^*)T^* \quad (7)$$

(4) Since λ and $\ln\dot{\varepsilon}^*$ exhibit a linear correlation, the intercept and slope obtained from the linear fitting of λ-$\ln\dot{\varepsilon}^*$ can be used to determine the values of λ_1 and λ_2, as shown in Step 3 in Fig.5. Hence, the specific expression of the modified Johnson-Cook model of the as-homogenized specimen is as follows:

$$\sigma = (77.93 + 20.78\varepsilon - 880.36\varepsilon^2 + 1327.53\varepsilon^3)(1 + 0.145\ln\dot{\varepsilon}^*)\exp[(-0.0048 + 5.99\times10^4\ln\dot{\varepsilon}^*)T^*] \quad (8)$$

$$\sigma = A\exp(n_1T)\varepsilon^{n_2}\dot{\varepsilon}^{*n_3}\exp\left(\frac{n_4}{\varepsilon}\right)(1+\varepsilon)^{n_5T}\exp(n_6\varepsilon)\dot{\varepsilon}^{*n_7T}T^{n_8} \quad (9)$$

where $n_1 - n_8$ and A are material parameters; T is the actual deformation temperature. To facilitate the solution of these

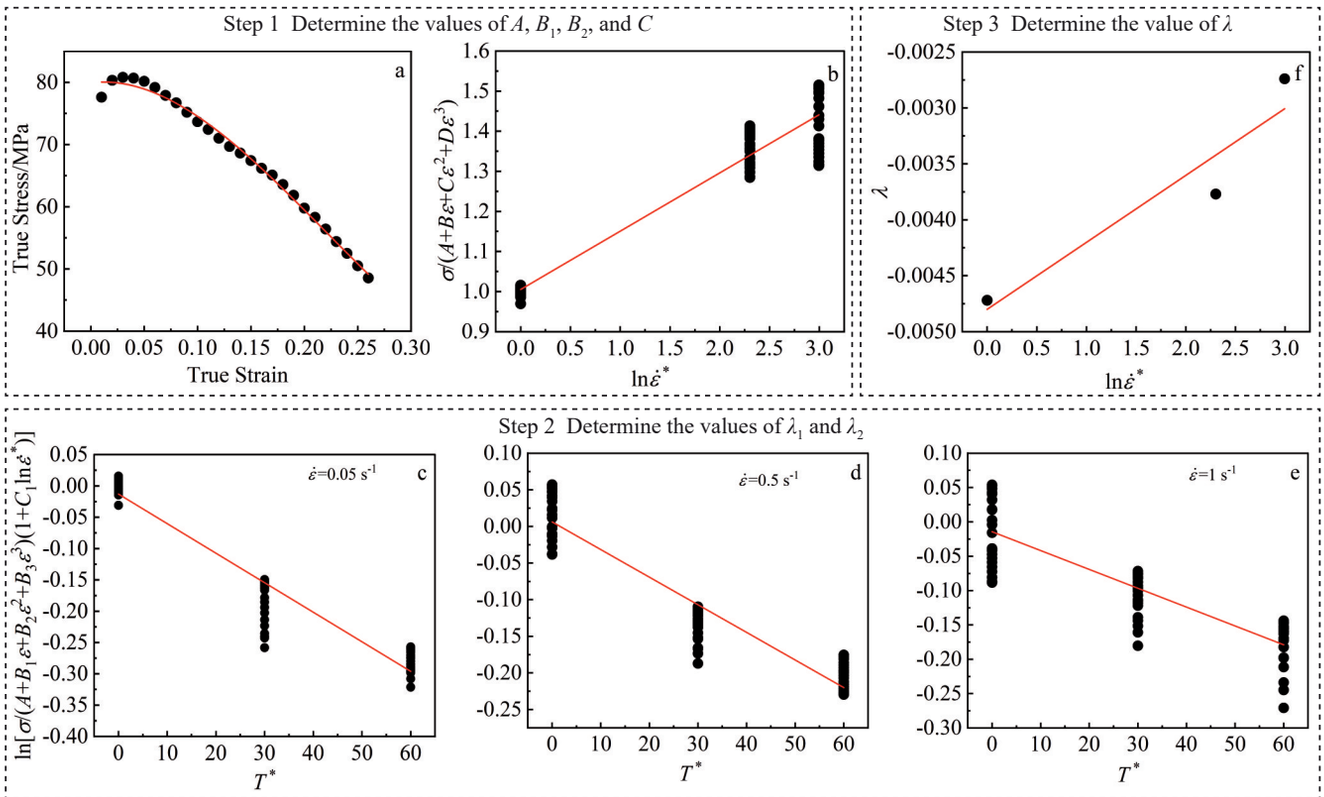

Fig.5 Solving processes of parameters in modified Johnson-Cook constitutive model

parameters, taking the logarithm of both sides of Eq.(9), and Eq.(10) is obtained, as follows:

$$\ln\sigma = \ln A + n_1 T + n_2 \ln\varepsilon + n_3 \ln\dot{\varepsilon}^* + \frac{n_4}{\varepsilon} + n_5 T\ln(1+\varepsilon) + n_6\varepsilon + n_7 T\ln\dot{\varepsilon}^* + n_8 \ln T \quad (10)$$

The parameters can be quickly determined through multiple linear regressions among lnσ, T, lnε, ln$\dot{\varepsilon}$, $1/\varepsilon$, Tln$(1+\varepsilon)$, ε, Tln$\dot{\varepsilon}$, ln$T$, and lnσ, as shown in Eq.(9). The parameters of the Hensel-Spittel model for as-homogenized Al-Zn-Mg-Cu alloy are listed in Table 4.

3.2.4 Strain-compensated Arrhenius model

The strain-compensated Arrhenius model exhibits different expressions for various stress levels, as follows:

$$\dot{\varepsilon} = \begin{cases} A\sigma^{n'}\exp(-Q/RT) & \alpha\sigma < 0.8 \\ A\exp(\beta\alpha)\exp(-Q/RT) & \alpha\sigma > 1.2 \\ A[\sinh(\alpha\sigma)]^n\exp(-Q/RT) & \text{for all } \sigma \end{cases} \quad (11)$$

where $\dot{\varepsilon}$ is the strain rate (s^{-1}); σ is the flow stress (MPa); Q is the deformation activation energy ($kJ\cdot mol^{-1}$); R is the gas mole constant (8.314 $J\cdot mol^{-1}\cdot K^{-1}$); T is the thermodynamics temperature (K); α , β , A, n', and n are material parameters with $\alpha = \beta/n'$. For example, when the strain is 0.05, the determination of parameters in the peak stress of as-homogenized specimen is obtained by the following processes, and results are shown in Fig.6.

(1) Taking logarithms on both ends of the equation for the high and low stress level states, Eq.(12) is obtained:

$$\begin{cases} \ln\dot{\varepsilon} = \ln A + n'\ln\sigma - Q/RT \\ \ln\dot{\varepsilon} = \ln A + \beta\sigma - Q/RT \end{cases} \quad (12)$$

From Eq. (12), lnσ exhibits a linear relationship with both lnσ and σ, whereas n' and β represent the reciprocals of the slopes of ln$\dot{\varepsilon}$ - lnσ and ln$\dot{\varepsilon}$ - σ. The fitted plots of ln$\dot{\varepsilon}$ - lnσ and ln$\dot{\varepsilon}$ - σ are obtained by linear regression, and the mean of the slopes is taken as the reciprocal. Therefore, the results are n' =7.0889, β=0.8535, and α=0.012 at the peak stress level.

(2) Taking the logarithm on the equation for all stress states.

$$\ln\dot{\varepsilon} = \ln A + n\ln[\sinh(\alpha\sigma)] - Q/RT \quad (13)$$

As depicted in Step 2 of Fig.6, the results are obtained, as follows: n=5.4169 and Q=113.023 $kJ\cdot mol^{-1}$.

The Z-parameter[30] effectively describes the coupling relationship between deformation temperature and strain rate during metal deformation and modifies the Arrhenius model.

$$\ln Z = \ln A + n[\ln\sinh(\alpha\sigma)] \quad (14)$$

Therefore, the resulting slope of the fitted line is n=5.41, and the intercept is ln$A$=17.4113.

The traditional Arrhenius model does not consider strain

Table 4 Parameter values of Hensel-Spittel model for as-homogenized Al-Zn-Mg-Cu alloy

ln$A$	n_1	n_2	n_3	n_4	n_5	n_6	n_7	n_8
180.82	0.042	0.298	−0.26	0.002 8	0.002 7	−6.21	0.000 58	−31.28

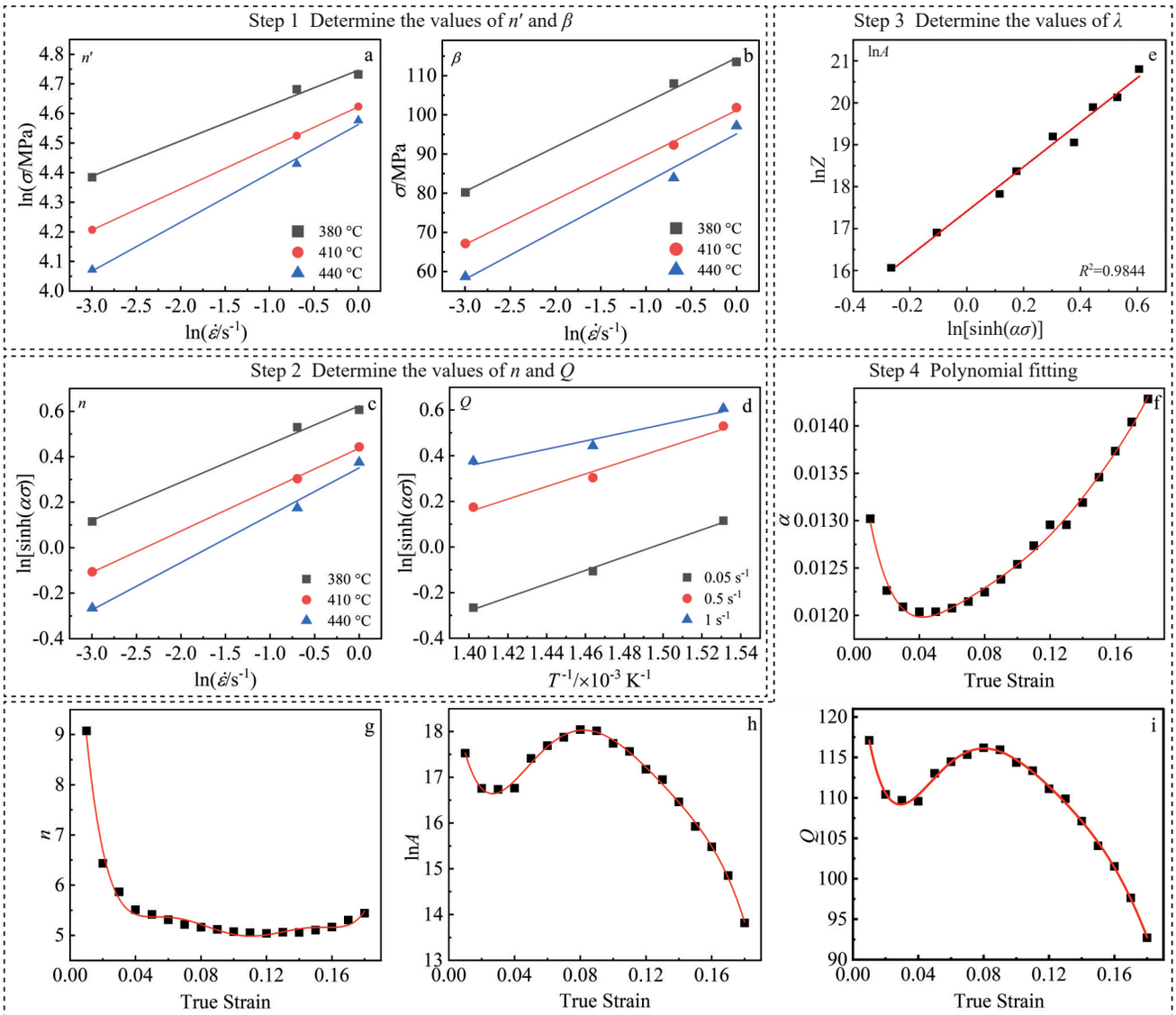

Fig.6 Solving processes of parameters of strain-compensated Arrhenius model

as a variable, so the incorporation of strain compensation can enhance the model accuracy. A sixth-order polynomial was used to obtain the parameters α, n', ln$A$, and Q, and the fitting curves are shown in Step 4 of Fig. 6. The strain-compensated Arrhenius model for the as-homogenized specimen is expressed by Eq.(15), as follows:

$$\begin{cases} \sigma = \dfrac{1}{\alpha(\varepsilon)} \ln\left\{\left[\dfrac{Z}{A(\varepsilon)}\right]^{\frac{1}{n(\varepsilon)}} + \left[\dfrac{Z}{A(\varepsilon)}^{\frac{2}{n(\varepsilon)}} + 1\right]^{\frac{1}{2}}\right\} \\ Z = \dot{\varepsilon} \exp\left(Q/RT\right) \end{cases} \tag{15}$$

3.2.5 Evaluation of model precision

Fig. 7 illustrates the comparison between predicted and experimental values across various models. It is evident that the Johnson-Cook model fails to adequately describe the high-temperature flow behavior of the Al-Zn-Mg-Cu alloy, which is constrained by the reference conditions of the model. For the Hensel-Spittel model, significant errors are observed within the low strain range during the deformation of as-homogenized specimen. In contrast, the data points of strain-compensated Arrhenius model closely align with the curve, indicating that this model can accurately predict the flow stress of both as-homogenized and as-rolled specimens.

This study employs the Pearson correlation coefficient R and the AARE to quantitatively evaluate the predictive accuracy of the constitutive model, as expressed by Eq. (16 – 17), respectively. The results are shown in Fig. 8a. It can be seen that the strain-compensated Arrhenius model exhibits good prediction accuracy with correlation coefficient of 0.9936 and 0.9967 for as-homogenized and as-rolled specimens, respectively. Notably, the Arrhenius model demonstrates a relatively lower AARE value of 2.15% for the flow stress data of the as-rolled specimen, compared with that of the as-homogenized specimen. Fig. 8b – 8d present correlation analysis plots of predicted and experimental values obtained by the Johnson-Cook model, Hensel-Spittel model, and

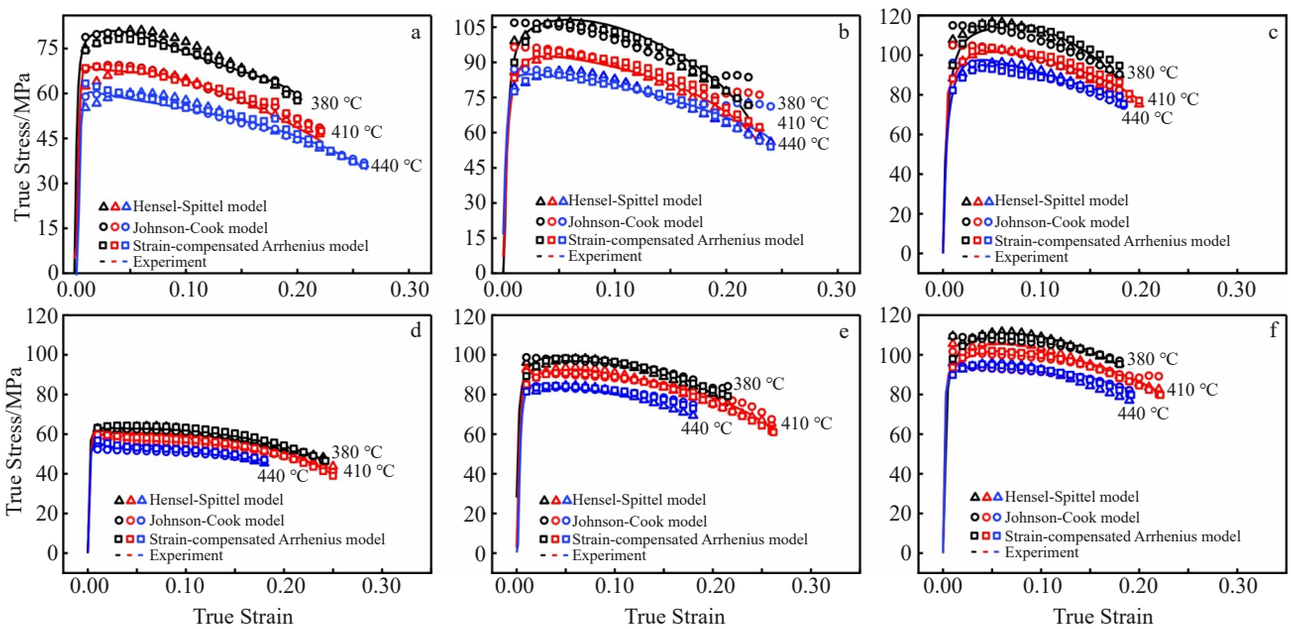

Fig.7 Comparison of experimental and predicted true stress obtained by different constitutive models of as-homogenized (a–c) and as-rolled (d–f) Al-Zn-Mg-Cu alloys under different strain rates: (a, d) $\dot{\varepsilon}$=0.05 s^{-1}; (b, e) $\dot{\varepsilon}$=0.5 s^{-1}; (c, f) $\dot{\varepsilon}$=1 s^{-1}

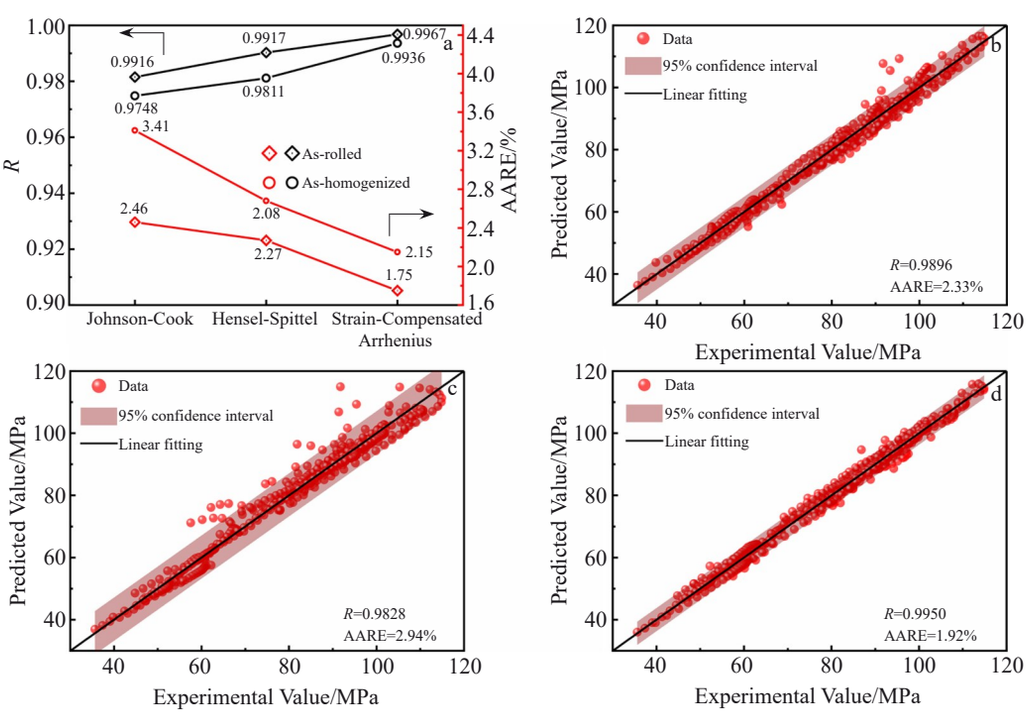

Fig.8 Variation curves of *R* and AARE values of different models for as-homogenized and as-rolled Al-Zn-Mg-Cu alloys (a); correlation plots between experimental and predicted values obtained by Johnson-Cook model (b), Hensel-Spittel model (c), and strain-compensated Arrhenius model (d)

strain-compensated Arrhenius model, respectively, and the shaded areas represent the 95% confidence intervals. In Fig. 8b, the Johnson-Cook model shows a large number of predicted data points deviating from the experimental values, demonstrating the widest confidence interval range in this research. Conversely, the strain-compensated Arrhenius model in Fig. 8d exhibits a convergent confidence interval with a correlation coefficient of 0.9950 and AARE value of 1.92%. This result further substantiates that the strain-compensated Arrhenius model can precisely describe the hot deformation behavior of as-homogenized and as-rolled specimens.

$$R = \frac{\sum_{i=1}^{n}(E_i - \overline{E})(P_i - \overline{P})}{\sqrt{\sum_{i=1}^{n}(E_i - \overline{E})^2\left[\sum_{i=1}^{n}(P_i - \overline{P})^2\right]}} \quad (16)$$

$$\mathrm{AARE} = \frac{1}{n}\sum_{i=1}^{n}\left|\frac{E_i - P_i}{E_i}\right| \times 100\% \quad (17)$$

where E_i represents the experimental value, $\bar{E}$ denotes the mean of the experimental values, P_i indicates the predicted value, $\bar{P}$ stands for the mean of the predicted values, and n signifies the number of experimental values in this study.

3.3 Microstructure and fracture morphology

Fig. 9 shows the inverse pole figures (IPFs) and kernel average misorientation (KAM) maps of the small-strain and large-strain areas in both the as-homogenized and as-rolled specimens subjected to hot tensile deformation under 410 °C/0.05 s^{-1} condition. Shear bands are evident in Fig. 9a and 9c, indicating the small- and large-strain areas in the as-homogenized specimen with the Von Mises strains ranging from 0.06 to 0.13 and from 0.38 to 0.47, respectively, and the simulation results are shown in Fig. 9i – 9j. Shear bands commonly appear in the aluminum alloys when the continuous dynamic recrystallization (DRX) process is incomplete[31], potentially arising from restricted dislocation diffusion rates. This phenomenon can be attributed to the presence of large secondary-phase particles, which impedes the dislocation movement, leading to high yield stress and low fracture elongation. This result is consistent with the true stress-true strain curves in Fig. 3. In contrast, Fig. 9b and 9d depict IPFs of small- and large-strain areas in the as-rolled specimen subjected to hot tensile deformation under 410 °C/0.05 s^{-1} condition. A more pronounced presence of refined grains along the grain boundaries is evident. This phenomenon is indicative of typical discontinuous DRX[32–34]. Furthermore, KAM values for the as-homogenized specimen are significantly higher than those of the as-rolled specimen. This phenomenon can be attributed to the pre-existing substructures within the as-rolled specimen, which offer additional sites for the absorption of newly generated dislocations through the rotation of substructures, DRX, and dynamic recovery. Besides, KAM values are decreased with the increase in strain for both the as-homogenized and as-rolled specimens. This should be attributed to the heat generation resulting from deformation, which elevates the local temperature of the specimen, subsequently promoting dynamic softening as strain increases.

As shown in Fig.10a and 10a_1, the microstructures of the as-homogenized specimen deformed under 380 ° C/0.05 s^{-1} condition exhibits unevenly distributed equiaxed dimples on the fracture surface, which is the characteristic of ductile fracture. Some secondary-phase particles are attached to the inner walls of the dimples, potentially acting as nucleation sites for microvoid formation.

In Fig.10a_1, bright river patterns can be observed, indicating typical brittle fracture. This phenomenon suggests that the ingot exhibits a mixed fracture mechanism rather than sole ductile or brittle fracture. As depicted in Fig.10d and 10d_1, the macroscopic fracture area diminishes in the fracture

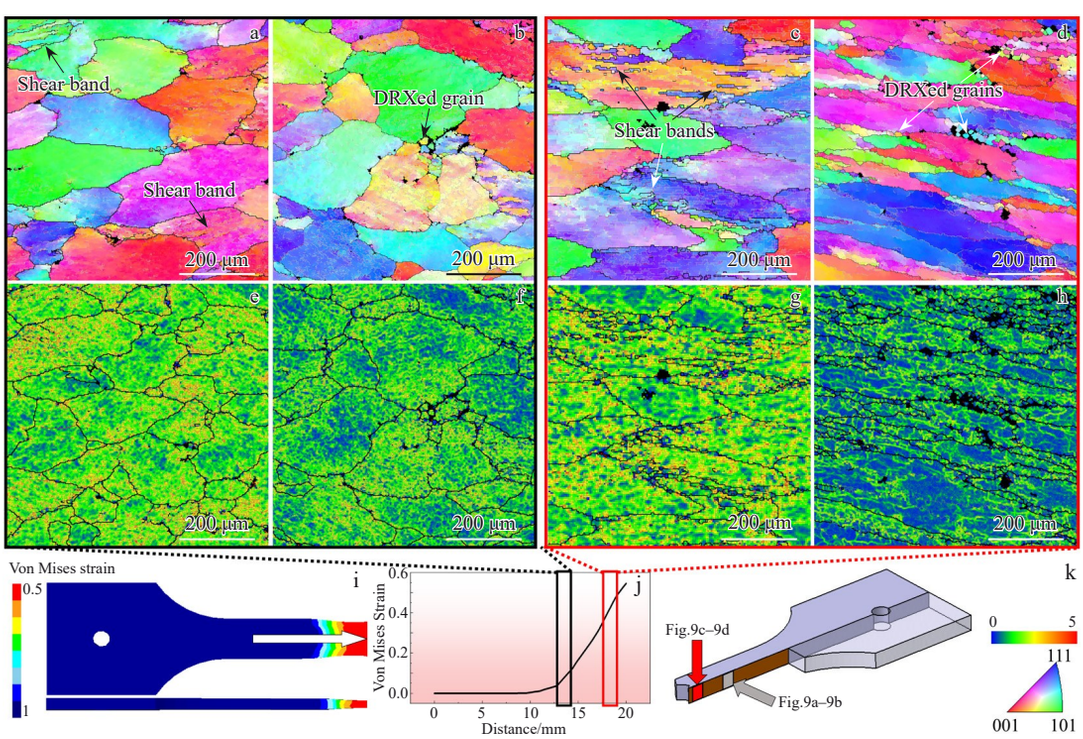

Fig.9 IPFs (a–d) and KAM maps (e–h) of small-strain (a–b, e–f) and large-strain (c–d, g–h) areas of as-homogenized (a, c, e, g) and as-rolled (b, d, f, h) specimens subjected to hot tensile deformation under 410 °C/0.05 s^{-1} condition; schematic diagram (i) and results (j) of simulated Von Mises strain distribution (i); schematic diagram of observation areas corresponding to Fig.9a–9d (k)

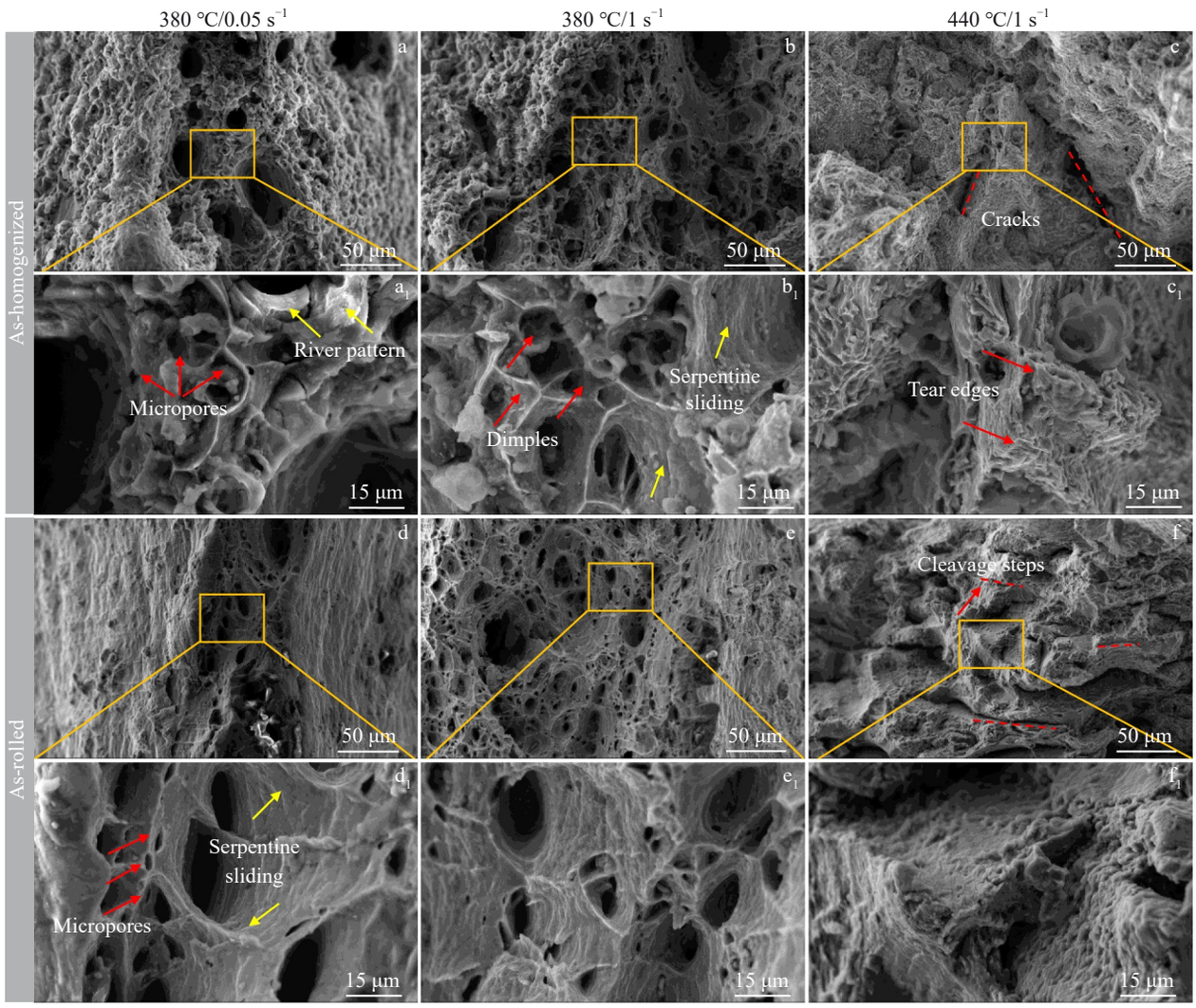

Fig.10 SEM morphologies of fracture surfaces of as-homogenized (a–c, a_1–c_1) and as-rolled (d–f, d_1–f_1) Al-Zn-Mg-Cu alloys subjected to hot tensile deformation under different conditions: (a, a_1, d, d_1) 380 °C/0.05 s^{-1}; (b, b_1, e, e_1) 380 °C/1 s^{-1}; (c, c_1, f, f_1) 440 °C/1 s^{-1}

morphologies of the as-rolled specimen, pronounced necking phenomenon occurs, and plastic deformation is further enhanced. The dimples become larger and deeper with noticeable serpentine slip patterns on the walls. Microvoids predominantly form in subgrain boundary regions, indicating the dominance of ductile fracture at this stage. Notably, strain rate and deformation temperature also affect the fracture characteristics. When the strain rate increases from 0.05 s^{-1} (Fig. 10a and 10d) to 1 s^{-1} (Fig. 10b and 10e), both fracture morphologies exhibit a trend of increased microvoids and dimples. This phenomenon is attributed to the incomplete migration of dislocations and grain boundary sliding at high strain rates, and the dimples and microvoids do not have sufficient time to further expand and grow. When the deformation temperature rises from 380 °C (Fig. 10b and 10e) to 440 °C (Fig. 10c and 10f), the softening effect at high temperatures leads to the disappearance of dimples and tear ridges[35]. The observed cleavage steps in the as-rolled specimen indicate the presence of localized brittle fracture.

3.4 Processing maps

Based on the dynamic material model (DMM), processing maps can characterize the thermal deformation behavior of materials by coupling the power dissipation coefficient and the instability criterion coefficient, which can describe the microstructure evolution characteristics and the changes in instability state during high-temperature deformation, which is typically used to predict the intrinsic workability of materials[36–38]. According to Ref. [39], the power dissipation coefficient η describes the proportion of energy consumed by the material under certain deformation conditions relative to the total energy dissipation. This indicator is positively correlated with the workability of the material[40], and it is related to the strain rate sensitivity factor m. The larger the positive value of m, the higher the plasticity value. The calculation formulas for m and η are represented by Eq.(18–20), respectively.

$$m = \frac{\partial \ln \sigma}{\partial \ln \dot{\varepsilon}} = b + 2c \ln \dot{\varepsilon} + 3d (\ln \dot{\varepsilon})^2 \quad (18)$$

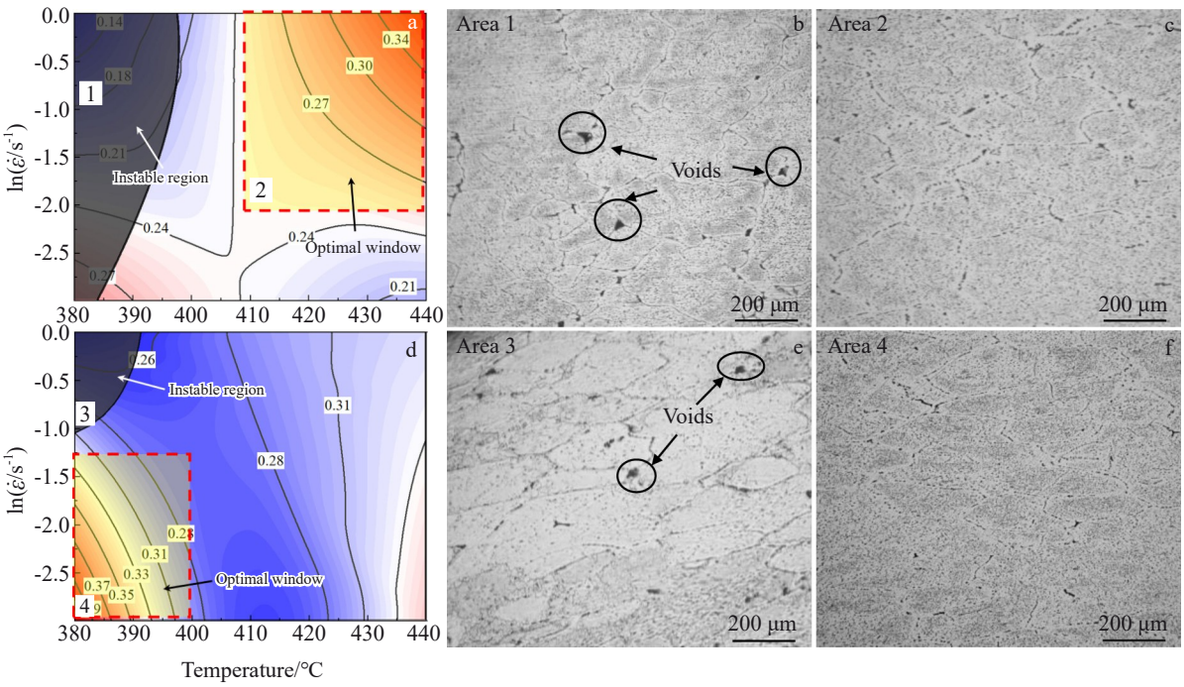

Fig.11 Processing maps at strain of 0.05 for as-homogenized (a) and as-rolled (d) Al-Zn-Mg-Cu alloys at peak tensile strain rate of 0.05 s^{-1}; OM images corresponding to area 1 (b), area 2 (c), area 3 (e), and area 4 (f) in Fig.11a and 11d

$$\eta = \frac{2m}{m+1} \tag{19}$$

where b, c, and d are related parameters.

It is essential to keep the η value within the stable region, as damage can occur in high-power dissipation areas[41]. Thus, it is necessary to identify the onset of process instability. In DMM, the instability criterion[42] is frequently used, as follows:

$$\zeta(\dot{\varepsilon}) = \frac{\partial \ln\left(\frac{m}{m+1}\right)}{\partial \ln \dot{\varepsilon}} + m < 0 \tag{20}$$

When $\zeta(\dot{\varepsilon}) < 0$, the internal deformation of the material is unstable. The cause of the instability is often the initiation of internal damage within the material, such as voids and cracks[43]. A lower value indicates a higher possibility of material instability. The superposition of contour plots depicting power dissipation and instability coefficients can intuitively delineate the flow safety and instability regions of materials under deformation conditions. High values of η and $\zeta(\dot{\varepsilon}) < 0$ often represent defect-free microstructure characteristics of the material[43], thereby identifying the optimal hot working window.

Fig. 11a and 11d illustrate the processing maps for the as-homogenized and as-rolled Al-Zn-Mg-Cu alloys at a peak tensile strain rate of 0.05 s^{-1}, respectively. Instable zones are evident in both specimens. In Fig. 11a, the power dissipation coefficient is increased with the increase in temperature when the strain rate exceeds 0.2 s^{-1}, and the instability zone is observed at 380–400 °C/0.05–1 s^{-1} region. With high temperatures and high strain rates, the as-homogenized specimen with η>0.25 has a processing safety zone. The optimal hot processing window for the as-homogenized specimen at the strain of 0.05 is determined to be 410–440 °C/0.14–1 s^{-1}. Fig. 11d shows that the instability region of the as-rolled specimen is reduced to 380–395 °C/0.37–1 s^{-1}, and the processing window is enlarged. Thus, the optimal hot processing window is identified as 380–400 °C/0.05–0.29 s^{-1}.

For the as-homogenized specimens, the presence of the coarse phase requires a relatively high temperature for the dislocation climb and grain boundary migration, and a moderate strain rate helps to balance the strain hardening and thermal softening. In the as-rolled specimens, DRX introduced by rolling reduces the temperature, and then the dynamic softening occurs. A low strain rate provides sufficient time for dislocation rearrangement to reduce flow instability.

Fig. 11b depicts the microstructures corresponding to the area 1 marked in Fig. 11a, which is within the unstable zone where voids are visible and deformation occurs at a higher strain rate. The majority of these voids are situated at the triple junctions of grain boundaries, which are susceptible to stress concentration. Additionally, bulk secondary-phase particles are located at these triple junctions (Fig. 1), enhancing stress concentration and diminishing plasticity. Fig. 11e also corresponds to the area within the unstable region, where voids can be observed. In contrast, Fig. 11c and 11f are situated in the optimal window, where no deformation defects exist and the deformation is relatively uniform.

4 Conclusions

1) The initial microstructure significantly influences the

flow characteristics. The as-rolled specimens have pre-existing substructures and fragmented secondary-phases, exhibiting enhanced activation of slip systems and reducing the barriers to dislocation movement. Consequently, these specimens demonstrate greater plasticity and lower deformation resistance, compared with the as-homogenized ones.

2) The strain-compensated Arrhenius model, which incorporates the fracture strain model, demonstrates the highest prediction accuracy for both as-homogenized and as-rolled Al-Zn-Mg-Cu alloys, achieving R value of 0.9950 and AARE value of 1.92%.

3) Shear bands and DRXed grains are the representative characteristic features of as-homogenized and as-rolled specimens, respectively. The fracture of as-homogenized and as-rolled specimens is dominated by mixed fracture mechanisms and ductile fracture mechanism, respectively.

4) The unstable region in as-rolled specimens is notably diminished. The optimal working window changes from $410-440$ °C/$0.14-1$ s^{-1} for as-homogenized specimens to $380-400$ °C/$0.05-0.29$ s^{-1} for as-rolled specimens.

References

1 Long S, Xia R Z, Jiang Y P *et al. Materials Today Communications*[J], 2023, 37: 107570

2 Wang L J, Li X Q, Pan C L *et al. Rare Metal Materials and Engineering*[J], 2023, 52(3): 867

3 Qi Y S, Jin Y, Wei F M *et al. Rare Metal Materials and Engineering*[J], 2025, 54(2): 327

4 El-Shenawy E, Farahat A I Z, Ragab A E *et al. Metals*[J], 2023, 13(7): 1158

5 Scharifi E, Yardley V A, Weidig U *et al. Advanced Engineering Materials*[J], 2023, 25(16): 2300141

6 Liu T, Jiang H T, Sun H *et al. Materials Science and Engineering A*[J], 2022, 847: 143342

7 Wang Z, Qi L, Wang G *et al. Mechanics of Materials*[J], 2016, 102: 90

8 Fan J, Ma M, Zhang K *et al. Journal of Rare Earths*[J], 2022, 40: 831

9 Derazkola H A, Garcia E, Murillo-Marrodán A *et al. Journal of Materials Research and Technology*[J], 2022, 18: 2993

10 Yao W Y, Bu H Y, Zhou S Q *et al. Materials Today Communications*[J], 2024, 38: 107861

11 Tan J Q, Zhan M, Liu S *et al. Materials Science and Engineering A*[J], 2015, 631: 214

12 Wang M L, Chen Z, Chen D *et al. Key Engineering Materials*[J], 2014, 575: 11

13 Wang S, Hou L, Luo J *et al. Journal of Materials Processing Technology*[J], 2015, 225: 110

14 Li C Y, Huang G J, Cao L F *et al. Metals and Materials International*[J], 2021, 27: 1

15 Chen S Y, Chen K H, Peng G S *et al. Transactions of Nonferrous Metals Society of China*[J], 2013, 23(4): 956

16 Guo L L, Zhang L N, Andersson J *et al. Journal of Materials Engineering and Performance*[J], 2024, 34: 6926

17 Wang C Y, Xu J S, Chen X *et al. Mechanics of Time-Dependent Materials*[J], 2023, 28: 2085

18 Wu H Y, Yu H Y. *Journal of Materials Engineering and Performance*[J], 2024, 34: 1

19 Lin Y C, Huang J, Li H B *et al. Vacuum*[J], 2018, 157: 83

20 Sun C Y, Qin Y, Liu Y *et al. Materials*[J], 2024, 17(5): 991

21 Henke T, Bambach M, Hirt G. *The 14th International ESAFORM Conference on Material Forming: ESAFORM 2011*[C]. Belfast: AIP Conference Proceedings, 2011, 1353(1): 71

22 Hensel A, Spittel T. *Kraft-Und Arbeitsbedarf Bildsamer Formgebungsverfahren*[M]. Leipzig: Deutscher Verlag fur Grundstoffindutrie, 1978

23 Yang Yang, Wang Weijun, Yang Liu *et al. Rare Metal Materials and Engineering*[J], 2025, 54(2): 517 (in Chinese)

24 Liu L, Zhao G, Wang G *et al. Journal of Materials Research and Technology*[J], 2023, 27: 3191

25 Wu S S, Zhu B H, Jiang W *et al. Materials*[J], 2022, 15(19): 6769

26 Johnson G R. *Proceedings of the 7th International Symposium on Ballistics*[C]. Hague: International Ballistics Committee, 1983

27 Zhi Huidong, Guo Baoquan, Ding Ning *et al. Rare Metal Materials and Engineering*[J], 2025, 54(3): 714 (in Chinese)

28 Lin Y C, Chen X M, Liu G *et al. Materials Science and Engineering A*[J], 2010, 527(1–2): 6980

29 Shokry A, Gowid S, Mulki H *et al. Materials*[J], 2023, 16(4): 1574

30 Zener C, Hollomon J H. *Journal of Applied Physics*[J], 1944, 15: 22

31 Long S, Jiang Y P, Xia R Z *et al. Materials Characterization*[J], 2024, 208: 113640

32 Zhong X T, Huang L K, Lei W *et al. Transactions of Nonferrous Metals Society of China*[J], 2018, 28(11): 2294

33 Sakai T, Miura H, Goloborodko A *et al. Acta Materialia*[J], 2009, 57: 153

34 Huang K E, Logé R E. *Materials and Design*[J], 2016, 111: 548

35 He D, Chen S B, Lin Y C *et al. Materials Today Communications*[J], 2023, 34: 105209

36 Wang Xianjun, Yang Junzhou, Wang Shichen *et al. Rare Metal Materials and Engineering*[J], 2024, 53(10): 2891 (in Chinese)

37 Wang H, Yin D F, Zhao M C *et al. Journal of Materials Research and Technology*[J], 2023, 27: 401

38 Miao J, Sutton S, Luo A A. *Materials Science and Engineering A*[J], 2020, 777: 139048

39 Prasad Y, Gegel H L, Doraivelu S M *et al. Metallurgical Transactions A*[J], 1984, 15: 1883

40 Reddy G J, Srinivasan N, Gokhale A A. *Journal of Materials Processing Technology*[J], 2009, 209(18–19): 5964

41 Prasad Y. *Journal of Materials Engineering and Performance*[J],

2003, 12: 638

42 Ziegler H. *An Introduction to Thermomechanics*[M]. Amsterdam: Elsevier, 2012

43 Wang Y Y, Zhao G, Xu X Y *et al. Journal of Alloys and Compounds*[J], 2019, 779: 735

初始显微组织状态对热拉伸变形过程中 Al-Zn-Mg-Cu 合金流动行为的影响

王姝俨[1]，周玉婷[2]，杜瑞博[3]，龙　帅[1,3]，林海涛[1]，王少阳[2]

(1. 西南铝业(集团)有限责任公司，重庆 401326)

(2. 中国航空工业集团公司 成都飞机工业(集团)有限责任公司，四川 成都 610073)

(3. 重庆科技大学 冶金与动力工程学院，重庆 401331)

摘　要：为研究 Al-Zn-Mg-Cu 合金均质态和轧态初始组织对拉伸流动行为的影响，在 GLEEBLE-3500 等温模拟器上进行温度范围为 380~440 ℃、应变率范围为 0.05~1 s^{-1} 的等温拉伸试验。建立了 Johnson-Cook 模型、Hensel-Spittel 模型、应变补偿的 Arrhenius 模型以及临界应变模型。结果表明：通过相关系数 R 和平均绝对相对误差评估模型，证明应变补偿的 Arrhenius 模型能更准确地代表合金的流动行为。在均匀化样品中剪切带更为明显，而在轧制样品中动态再结晶则占主导地位。断裂形态分析表明，均匀态试样中混合断裂机制占主导地位，而轧制试样中主要是延性断裂机制。加工图谱显示，与均匀态试样相比，轧态试样的不稳定区域减小，最优热加工窗口分别确定为 410~440 ℃/0.14–1.00 s^{-1} 和 380~400 ℃/0.05~0.29 s^{-1}。

关键词：Al-Zn-Mg-Cu 合金；拉伸流动行为；微观结构；本构建模；加工图

作者简介：王姝俨，女，1992 年生，硕士生，工程师，西南铝业(集团)有限责任公司，重庆 401326，E-mail：924537153@qq.com